machines

MDPI

Article

CFD Analysis on Novel Vertical Axis Wind Turbine (VAWT)

Chris Sungkyun Bang [1,*], Zeeshan A. Rana [2] and Simon A. Prince [3]

[1] Advanced Vehicle Engineering Centre, School of Aerospace, Transport and Manufacturing, Cranfield University, Cranfield MK43 0AL, UK
[2] Department of Mechanical Engineering, Prince Mohammad Bin Fahd University, Al-Khobar 31952, Saudi Arabia; zrana@pmu.edu.sa
[3] Centre for Aeronautics, School of Aerospace, Transport and Manufacturing, Cranfield University, Cranfield MK43 0AL, UK; simon.prince@cranfield.ac.uk
* Correspondence: chris.bang@cranfield.ac.uk

Abstract: The operation of vertical axis wind turbines (VAWTs) to generate low-carbon electricity is growing in popularity. Their advantages over the widely used horizontal axis wind turbine (HAWT) include their low tip speed, which reduces noise, and their cost-effective installation and maintenance. A Farrah turbine equipped with 12 blades was designed to enhance performance and was recently the subject of experimental investigation. However, little research has been focused on turbine configurations with more than three blades. The objective of this study is to employ numerical methods to analyse the performance of the Farrah wind turbine and to validate the findings in comparison with experimental results. The investigated blade pitch angles included both positive and negative angles of 7, 15, 20 and 40 degrees. The k-ω SST model with the sliding mesh technique was used to perform simulations of a 14.4 million element unstructured mesh. Comparable trends of power output results in the experimental investigation were obtained and the assumptions of mechanical losses discussed. Wake recovery was determined at an approximate distance of nine times the turbine diameter. Two large complex quasi-symmetric vortical structures were observed between positive and negative blade pitch angles, located in the near wake region of the turbine and remaining present throughout its rotation. It is demonstrated that a number of recognised vortical structures are transferred towards the wake region, further contributing to its formation. Additional notable vortical formations are examined, along with a recirculation zone located in the turbine's core, which is described to exhibit quasi-symmetric behaviour between positive and negative rotations.

Keywords: VAWT; Farrah wind turbine; computational analysis; vortical structures

Citation: Bang, C.S.; Rana, Z.A.; Prince, S.A. CFD Analysis on Novel Vertical Axis Wind Turbine (VAWT). *Machines* **2024**, *12*, 800. https://doi.org/10.3390/machines12110800

Academic Editor: Davide Astolfi

Received: 19 September 2024
Revised: 30 October 2024
Accepted: 5 November 2024
Published: 12 November 2024

1. Introduction

As a result of global warming and consequential climate change concerns, necessary actions to reduce their primary causes, such as greenhouse gas emissions and carbon footprint, have been taken by restricting the energy usage generated by fossil fuels and banning the sale of ICE (internal combustion engine) cars after 2035 [1]. One of the key resources to generate low-carbon electricity is renewable power, which is supported by the International Energy Agency, stating that 90% of electricity generation globally will come from renewable sources in 2050 [2]. According to the report [3], the significance of wind energy as a renewable source in the UK has been clearly demonstrated. The country boasts the largest offshore wind farm globally, and wind power contributes to 24% of the total electricity generation. This achievement can be attributed to the utilisation of horizontal axis wind turbines (HAWTs).

It is reported that roughly 90% of turbines currently in use are HAWT machines, making them the prevailing choice for electricity generation [4,5]. A wind turbine with a vertical rotor shaft and blades that revolve in a horizontal plane is known as a vertical axis wind turbine (VAWT). Cross-wind axis turbines, as they are commonly called, have

the ability to run on both drag and lift, whereas HAWT is solely dependent on drag. The usual performance curves for the two most popular VAWT variants are plotted against the most popular HAWT type in Figure 1. When it comes to large-scale industrial wind energy generation, HAWTs are typically chosen because of their comparatively high peak aerodynamic efficiency. Conversely, VAWT designs have the advantage of being less loud due to their lower tip speeds and being more cost-effective to build and operate for smaller-scale applications like water pumping in cities. Furthermore, the advantage of the VAWT is its capacity to handle wind flow in multiple directions, which might fluctuate constantly in residential areas and increase the machine's efficiency in turbulent flow regions [6–8].

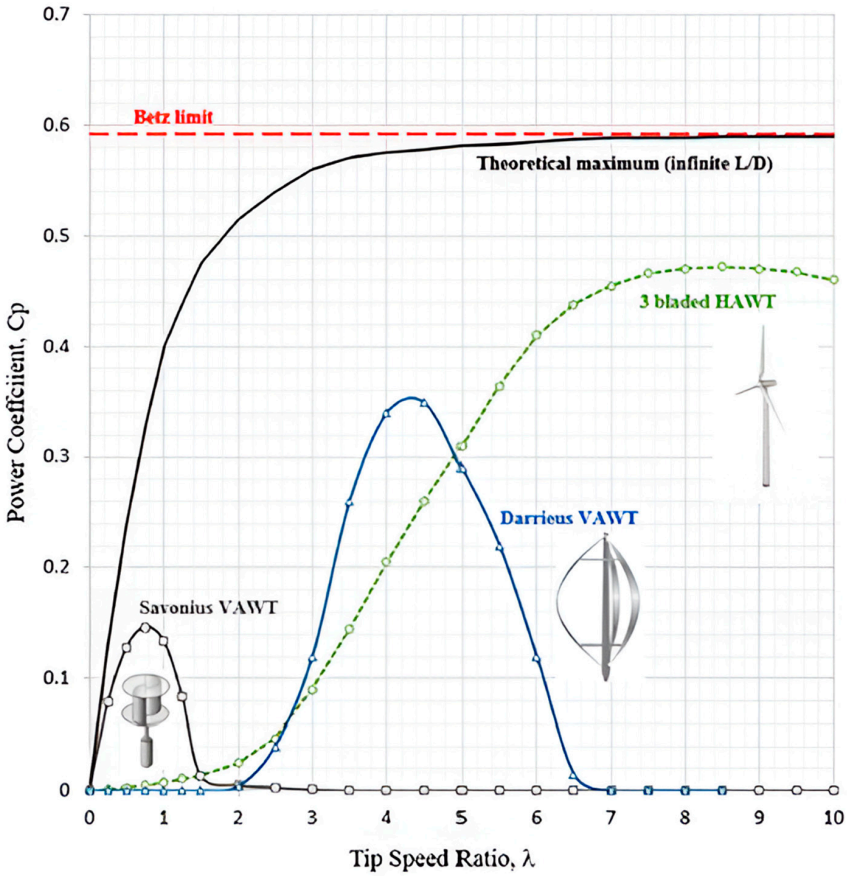

Figure 1. Performance characteristics for three popular designs of wind turbine [9].

The version of the VAWT credited to the Finnish engineer Savonius is the most basic [10,11]. The Savonius turbine, which is made up of a series of simple blades with a cross-section that resembles the letter 'S', is typically thought of as a drag-powered device because its power comes from the drag differential between the convex retreating blade and the concave advancing blade. The Bach-type Savonius turbine was developed to increase rotor efficiency by adding an overlap gap between the blades to provide airflow recirculation and an additional lift component. Several studies supported these findings experimentally and theoretically [12–18]. Further development of the VAWT was proposed and assessed by Austin Farrah in the early 1990s, illustrated in Figure 2. The plan was to create a vertical axis machine that would increase the turbine torque by utilising both the drag force of the blades and the leading edge suction produced by the profiled blades. He acknowledged that a mechanical system that would provide a cyclic motion to the blades as they revolved around the central axis would be advantageous. There is no information about the reason why Farrah selected 12 blades; however, it represents a balance between various factors such as aerodynamic considerations (Reynolds number based on blade chord, the trailing edge gap size, etc.) and the complexity and cost associated

with structural design and manufacturing. Prince et al. [19] provided a detailed assessment of the performance merits of the Farrah turbine concept in comparison with a Bach-type Sanovius turbine, particularly evaluating the effect of blade pitch setting and the size of the cylinder on its performance through a carefully designed comparative wind tunnel test.

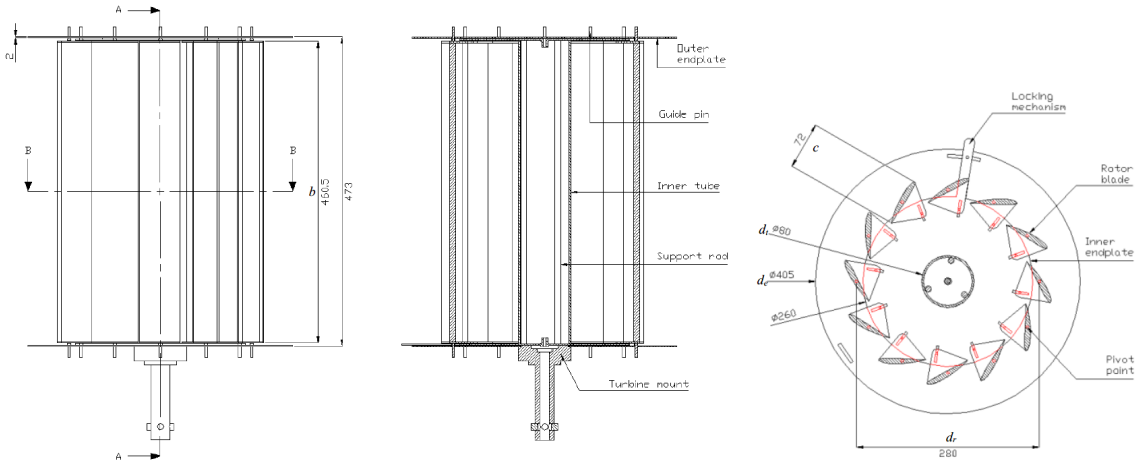

a) Side view *b) Section A-A* *c) Section B-B*

Figure 2. Schematics of Farrah wind turbine (dimensions in mm): (**a**) side view, (**b**) section A-A and (**c**) section B-B [19].

In recent years, numerical investigations based on computational fluid dynamics (CFDs) have been utilised in a wide range of industries to investigate flow features [20–24]. Likewise, computational analysis was applied to enhance the development of the VAWT concept effectively. This allowed for an adequate evaluation of its performance characteristics and a better comprehension of the complexity of flow structures with fewer resources and efforts [25]. Howell et al. studied a Darrieus turbine with straight vertical blades in both a two- and three-dimensional manner using a URANS (Unsteady Reynolds-Averaged Navier–Stokes) model, resulting in an overestimated performance level from 2D analysis [26]. In a comparable manner, Rossetti and Pavesi investigated the self-start capability of an H-blade Darrieus rotor and the importance of its three-dimensionality-related features including secondary flows and tip effects, which were demonstrated to increase the reliability of numerical outcomes [27]. In order to enhance the accurate prediction of the performance of a VAWT using computational analysis, Rezaeiha et al. provided useful guidelines regarding the domain size and azimuthal increment by carrying out CFD simulations with URANS [28,29]. Elkhoury et al. employed more sophisticated turbulence models such as Large Eddy Simulation (LES) and Delay Detached Eddy Simulation (DDES) to investigate the performance of a three-bladed O-VAWT, which was found to adequately predict the output power along with the associated three-dimensional vortical flow structures [30,31]. In a similar manner, to improve prediction accuracy compared to experimental data, a new DDES model with an adaptive coefficient (DDES-AC) was proposed, capturing dynamic stalls occurring around aerofoil trailing edges [32].

As mentioned in the preceding paragraph, the computational approach has been widely employed to effectively investigate the aerodynamic performance of Vertical Axis Wind Turbines (VAWTs). However, the majority of publications have concentrated on VAWTs with two or three blades, with only a limited number of studies examining turbine configurations beyond these blade numbers. The presented work aims to numerically investigate the performance characteristics of the Farrah-type wind turbine and to validate the computational findings through a comparison with experimental results obtained by Prince et al. [19], where the experimental data were recorded using the 'T7 low-speed wind tunnel' of City University London, in order to demonstrate its ability to investigate the performance of such a type of turbine.

2. Materials and Methods

This section details the methodology conducted for the construction of the VAWT numerical model presented above. The methodology section is divided into the following subsections: meshing, boundary conditions, simulation setup and the numerical cases with reference to the data provided by Prince et al. [19].

2.1. Meshing Strategy

2.1.1. Design Parameters

The geometrical design process of the VAWT was achieved through SpaceClaim 2021 R2 software, which we will now describe. Using the NACA 5 Series aerofoil online generator [33], we first imported airfoil coordinates (including 1000 points) and used a Bezier curve fit to define the surface. Following the importation of the airfoil, the trailing edge was chamfered and defined as two separate surfaces, as can be observed in Figure 3. This alteration supported greater orthogonality within the mesh generation of boundary layer cells and, as shown later, improved the geometrical representation of the mesh.

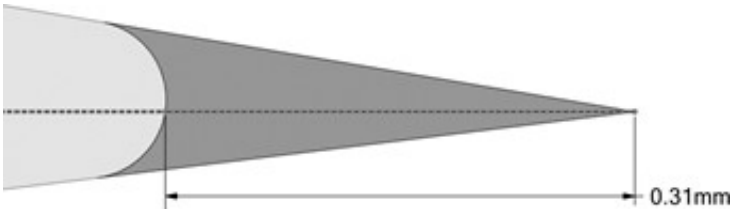

Figure 3. Blade aerofoil with trailing edge chamfered.

After the equidistant mirror/pattern and extrusion process, the geometry was exported in IGES file format, and an unstructured tetrahedral mesh was developed. The detailed geometry of the domain and turbine is shown in Figure 4 and Figure 5, respectively.

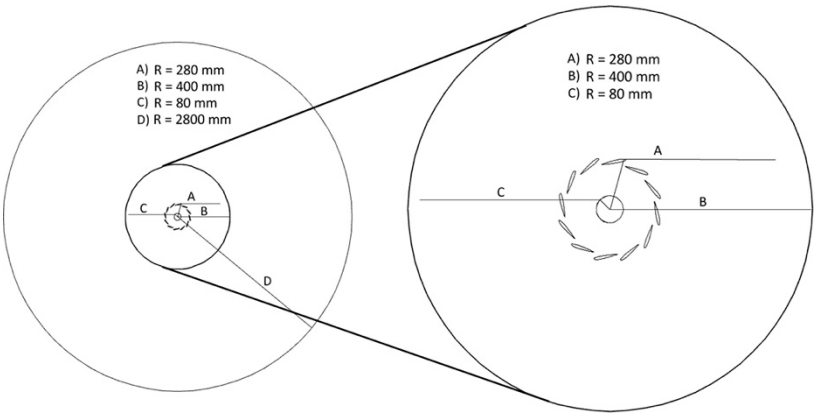

Figure 4. Dimensions of domain.

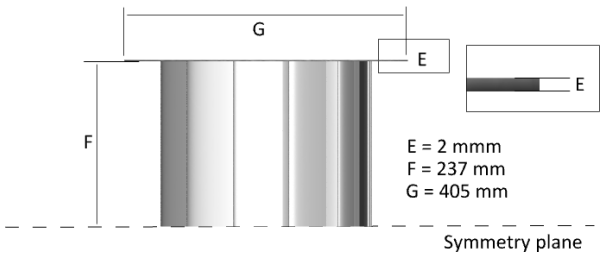

Figure 5. Dimensions of turbine.

2.1.2. Mesh Parameters

The creation of a unified mesh representation of all the specified blade pitch angles was initially developed from the maximum angle of positive 40 degrees. Using Pointwise V18.4 R4 software, three meshes of coarse, medium and fine resolution were generated with properties stated in Table 1, as visualised in Figure 6. The grid independent study was carried out using the meshes with the k-ω SST turbulence model, monitoring the power output displayed in Table 2. These values correspond when the 12 airfoils are treated either as a single boundary condition or various wall boundary conditions (12 in this case). In a similar manner, in Table 3, the results are presented when using the Spalart–Allmaras (S-A) model.

Table 1. Comparison of grid resolution.

Mesh Properties	**Mesh Definitions**		
	Coarse	**Medium**	**Fine**
Cell count	3,603,118	7,243,248	14,438,984
Number of cells (static mesh)	100,110	201,545	398,947
Number of cells (sliding mesh)	3,503,008	7,041,703	14,040,037
Number of points per airfoil	84	124	164
Leading edge spacing	0.8	0.6	0.1
Number of points (leading edge, +z)	200	400	600
Trailing edge spacing	0.2	0.2	0.2
Number of points (trailing edge, +z)	500	600	800
y+ (airfoil)	5	2	1
No. inflation layers	10	15	20
Initial layer height (cylinder)	0.2	0.1	0.05
Inflation layer growth rate	1.2	1.2	1.2
Block decay rate (sliding mesh)	0.5	0.55	0.65
Number of points (endplate)	100	100	100
Average spacing (farfield)	150	130	100
Number of cells (sliding mesh interface)	2034	4600	8199
Number of cells (static mesh interface)	1626	8428	14,484

Table 2. Power output and GCI results with different boundary conditions using k-ω SST model.

	Single BC	**Multiple BC**
Exp. power [W]	4.97	
Fine grid power [W]	2.64	4.77
Medium grid power [W]	2.99	4.67
Coarse grid power [W]	3.47	4.55
Order of convergence	0.466	0.353
Zero grid spacing value (power) [W]	1.74	5.11
GCI coarse	0.523	0.118
GCI fine	0.428	0.090
Asym. range	0.884	1.02

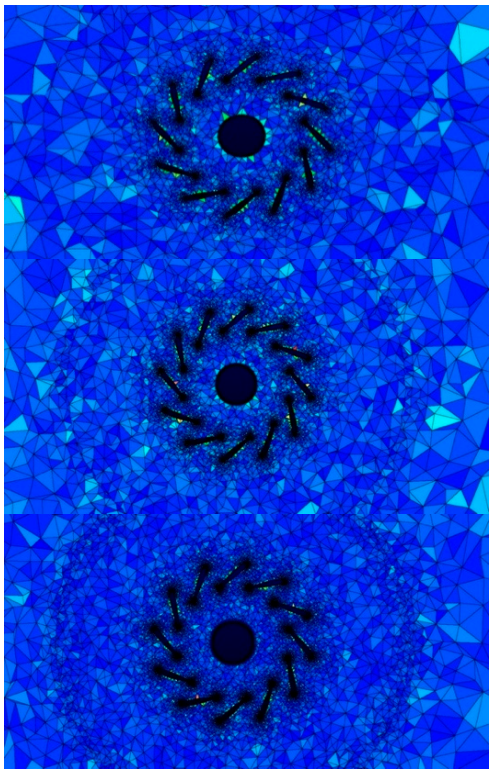

Figure 6. Volume ratio contours of grid generated: (**a**) coarse; (**b**) medium; (**c**) fine.

Table 3. Power output and GCI results with different boundary conditions using S-A model.

	Single BC	**Multiple BC**
Exp. power [W]	4.97	
Fine grid power [W]	1.51	2.82
Medium grid power [W]	1.79	2.79
Coarse grid power [W]	2.56	3.36
Order of convergence	1.457	4.535
Zero grid spacing value (power) [W]	1.35	2.82
GCI coarse	0.308	0.011
GCI fine	0.132	0.0005
Asym. range	0.844	1.013

As shown, differences within the boundary conditions are noticed. The initial identification of the model, represented as a connected wall, is shown to produce results whereby the torque corresponds to half of the VAWT. In contrast, when airfoil walls are defined separately, it is noticed that torque values show similar results to those found within the experimental reference [19]. From this study, the theoretical zero-spacing grid is identified through Richardson extrapolation. In addition, it can be seen that the estimation when using the S-A turbulence model has a considerable deviation from the experimental results, either modelling a single or multiple walls, with a minimum error of 43.25% for the fine mesh. In Figure 7, it is observed that the S-A model does not provide a sinusoidal torque signal as is the case for k-ω SST, since from previous works like Howell et al. [26], it is known that oscillations have to be present. Therefore, it is concluded that the k-ω SST model proved to be suitable for the current study.

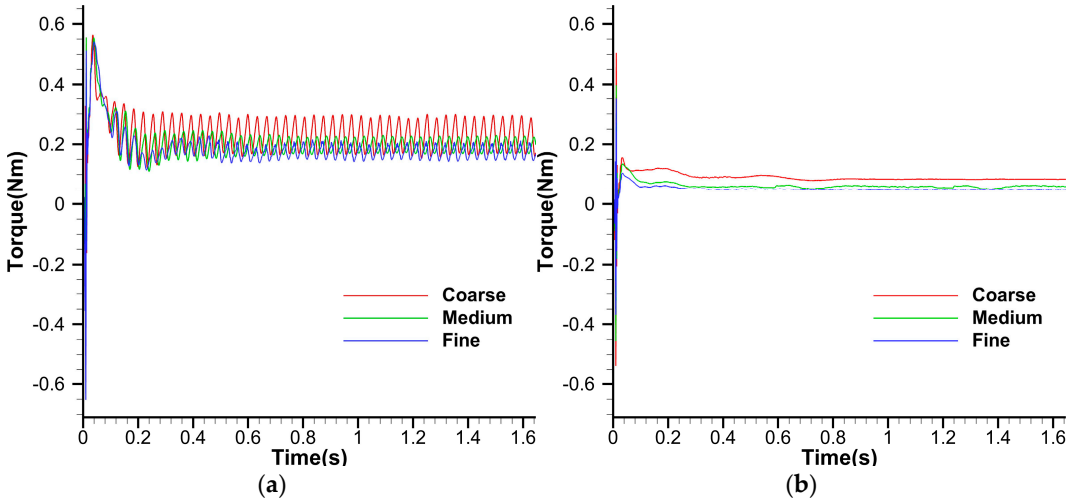

Figure 7. Overall torque curves over time, employing (**a**) k-ω SST model, (**b**) S-A model.

2.2. Boundary Conditions

Boundary conditions are applied to the computational domain, specifically to areas of the domain where known variables values can be implemented. Thus, these conditions allow us to initialise the problem, enabling us to solve the Navier–Stokes equations iteratively using the available CFDs algorithms. In this case study, four different boundary conditions are used, which are applied to the different limits that define the computational domain, as shown in Figure 8.

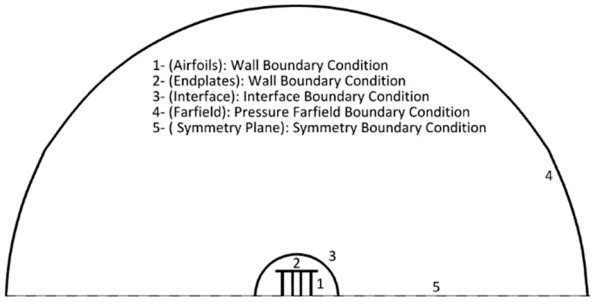

Figure 8. Boundary conditions for the computational domain.

The interface boundary condition is necessary to make the sliding mesh work, where a static fluid volume and a rotational fluid volume are required. This is why these two volumes (which are in contact) must have their interface defined with respect to the other volume, which is why it is essential to define two interfaces. The governing equation for this type of boundary is defined by the conservation equation for dynamic meshes [34], so that the following holds:

$$\frac{d}{dt}\int_V \rho\phi dV + \int_{\partial V} \rho\phi\left(\vec{u} - \vec{u}_g\right)\cdot d\vec{A} = \int_{\partial V} \Gamma\nabla\phi\cdot d\vec{A} + \int_V S_\phi dV \quad (1)$$

where

ρ is the fluid density,
$\vec{u}$ is the flow velocity vector,
$\vec{u}_g$ is the mesh velocity of the moving mesh,
Γ is the diffusion coefficient,
S_ϕ is the source term of ϕ.

The aforementioned equation allows for updating the flow in moving mesh zones, as long as an appropriate specification of the rigid mesh movement is defined for each

zone (a simple linear or rotational movement or even more complex movements); for this work, a simple rotational velocity specification has been implemented for sliding mesh [34]. Furthermore, as the mesh motion in the sliding mesh formulation is rigid, all cells conserve their original form and volume. Consequently, the time rate of change of the cell volume is zero, which gives the following:

$$V^{n+1} = V^n \tag{2}$$

The pressure farfield is a boundary condition applied to simulations where the boundaries are far enough away from the geometry in order for the flow to be developed, where the Navier-slip boundary condition is applied, in which the flow is considered to be tangential to the boundary. On the other hand, if these boundaries are not far enough away from the object, the boundaries are considered as inlet and outlet. This boundary condition is often used to derive the velocity or pressure in phantom cells of the domain, so that mass loss of the flow is avoided [35]. The International System (SI) default settings for this boundary condition are summarised in the following Table 4.

Table 4. International System (SI) default settings for pressure farfield boundary condition [34].

Gauge pressure [Pa]	0
Mach number	0.6
Temperature [K]	300
X-Component flow direction	1
Y-Component flow direction	0
Z-Component flow direction	0
Turbulent kinetic energy [J/kg]	1
Turbulent dissipation rate [J/(kg s)]	1

This boundary condition is a non-reflecting boundary condition based on the use of characteristic variables for a one-dimensional flow normal to the boundary (the boundary furthest from the body to be analysed), for which Riemann invariants are required [34]. For cases such as the present work, in which the dynamics of a subsonic flow are analysed, two Riemann invariants are used, corresponding to the incoming and outgoing waves.

For the following invariants, ∞ refers to the conditions at the infinity boundary, while i is the cell adjacent to the boundary, located in the interior of the domain. The formulations for these invariants are as follows:

$$R_\infty = v_{n\infty} - \frac{2a_\infty}{g-1} \qquad R_i = v_{ni} - \frac{2ai}{g-1} \tag{3}$$

where v_n is the normal velocity at the boundary condition, a is the speed of sound, and g is the ratio of specific heats, for which the ideal gas condition must be used for this boundary condition [34]. In this way, these two invariants can be related, giving rise to a mean normal velocity (v_n) and speed of sound (a) at the boundary, from which it is possible to calculate the value of the remaining variables in the boundary.

$$v_n = \frac{1}{2}(R_i + R_\infty) \qquad a = \frac{g-1}{4}(R_i - R_\infty) \tag{4}$$

The symmetry boundary condition is a condition that allows the simulation time to be reduced for cases in which the solution is expected to be symmetrical. This is why defining a computational domain such as the one in this case, where half of the wind turbine and half of the domain describing the fluid have been designed, can reduce the computational time considerably. In addition, the results of the complete turbine can be post-processed by applying a mirror condition and therefore showing the complete results, since the results are expected to be symmetrical with respect to the Z = 0 plane.

2.3. Simulation Setup

This subsection presents the selected parameters as an input to ANSYS Fluent 2021R2 in order to simulate the flow field around the Farrah turbine. The selected solver was a pressure-based type with a transient formulation; the RANS-based turbulence model was Menter's k-ω SST as, according to a literature review, it gives good results when studying VAWTs. It is important to note that when selecting the k-ω SST model, the enhanced wall treatment for the k equation was used; for fine meshes, the low-Reynolds formulation was applied [34].

The rotation of the turbine is achieved by using the sliding mesh method; hence, the CAD model of the turbine is immersed in a rotatory domain. The interface between the rotatory and static domain is set up as the matching type. Using a pressure farfield boundary implies the activation of the energy equation because the density of the fluid is computed by the ideal-gas law; the conditions of this boundary correspond to the air at P_{abs} = 101,325 Pa and T = 293.15 K. At a freestream Mach number of 0.06, even with some acceleration along the sides, the flow remains largely incompressible and the compressibility effects are negligible.

The discretisation of the variables is performed through second-order schemes and the least squares cell-based method is used to approximate the gradient. SIMPLEC is chosen as the pressure–velocity coupling scheme along with distance-based Rhie–Chow interpolation. A second-order implicit scheme is responsible for the transient formulation with the default value for high-order term relaxation.

An appropriate time step (Δt) must be used in order to avoid solution divergence; most of the literature converts Δt into an angular step Δθ so the time marching is independent of the angular velocity. Three-bladed VAWT studies like the one of Elkhoury et al. have used 1.2°—the most common is 1.0°—but it was shown by Lanzafame et al. that this may be insufficient and it should be reduced to 0.36°, a value similar to that used by Bianchini et al. when studying a six-bladed Darrieus turbine [30,36–39]. A value of 0.3° is adopted in the present investigation considering the high number of blades present in the Farrah turbine; 50 iterations are set per time step. The total simulated time corresponds to four revolutions, which is less than what was suggested by Rezaeiha et al. [29]; nonetheless, it has been observed that such a value provides a nice stable periodic torque output for such a number of revolutions. Most of the simulations were run on a high-performance computer at Cranfield University, Crescent, using 64 cores per case studied.

2.4. Numerical Cases

Referring to Prince's experimental work [19], positive and negative angles of 7°, 15°, 20° and 40° were taken into consideration for fair comparison. Thus, the following Table 5 is a summary of the cases that were considered.

Table 5. Summary of initial boundary conditions of cases from Prince's experiment [19].

	7°		**15°**		**20°**		**40°**	
	+7°	**−7°**	**+15°**	**−15°**	**+20°**	**−20°**	**+40°**	**−40°**
RPM-1	45.349	−45.349	83.057	−74.357	86.788	−88.069	95.546	−97.893
U [m/s]	14.89	14.890	12.615	12.180	10.962	11.086	9.445	9.346
dt [second]	0.00110	0.00110	0.00060	0.00067	0.00058	0.00057	0.00052	0.00051
Ma	0.04339	0.04339	0.03676	0.03549	0.03194	0.03230	0.02752	0.02723
RPM-2	57.873	−57.873	123.216	−106.136	150.050	−130.615	145.72	−151.953
U [m/s]	16.73	16.730	15.574	14.654	14.468	13.734	11.733	11.758
dt [second]	0.00086	0.00086	0.00041	0.00047	0.000333	0.000383	0.000343	0.00033
Ma	0.04875	0.04875	0.04538	0.04270	0.04216	0.04002	0.03419	0.03426

Table 5. *Cont.*

	7°		15°		20°		40°	
	+7°	**−7°**	**+15°**	**−15°**	**+20°**	**−20°**	**+40°**	**−40°**
RPM-3	70.199	−70.199	159.149	−137.242	196.659	−173.015	201.048	−200.766
U [m/s]	18.57	18.570	17.974	16.855	16.979	16.059	13.697	13.685
dt [second]	0.00071	0.00071	0.00031	0.00036	0.00025	0.00029	0.00025	0.00025
Ma	0.05411	0.05411	0.05237	0.04911	0.04947	0.04679	0.03991	0.03987
RPM-4	78.579	−78.579	194.855	−183.949	238.222	−224.654	254.965	−265.935
U [m/s]	19.872	19.872	19.876	19.842	18.960	18.588	15.712	15.971
dt [second]	0.00064	0.00064	0.00026	0.00027	0.00021	0.00022	0.00020	0.00019
Ma	0.05790	0.05790	0.05791	0.05781	0.05524	0.05416	0.04578	0.04654

3. Results

This chapter evaluates the results obtained from the simulations of our experiment. The parameters of power, torque, velocity, pressure, TKE and Q-criterion are presented using several different flow visualisation techniques. A comparison is made between high and low wind speeds, with 11.7 and 16.8 m/s termed as case 1 and case 2, respectively. Both blade orientations of 7° were not considered for the case 1 comparison, as it has been proven experimentally that the turbine is unable to rotate at this velocity. The positive and negative contours of 40° are shown as they generated the highest amount of torque among all blade pitch angles.

3.1. Power

The power estimated by the CFD model and its comparison with experimental data [19] is presented in Figures 9 and 10, where the only difference between results is the modelled magnitude of the mechanical losses. Figure 9 shows the power estimation when these losses account for 50% of the power output, and in Figure 10, these losses account for 20%. Regarding these losses, there is no clear understanding of the evolution of the energy dissipation for the current experimental setup. This raises a discussion about the suitability of the k-ω SST model.

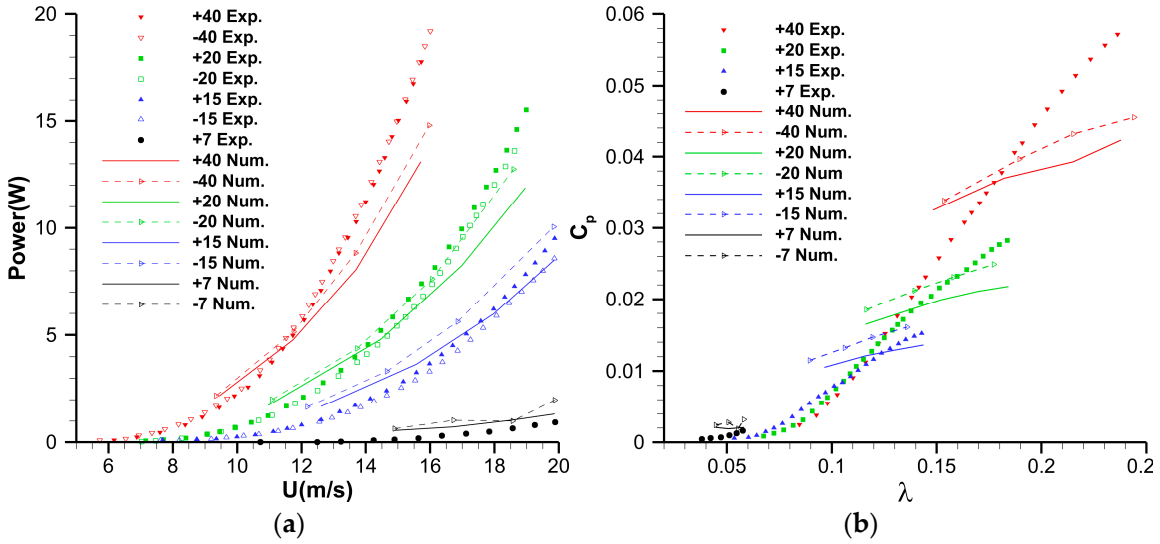

Figure 9. Estimation of turbine performance by CFDs model compared with experimental data when considering mechanical losses of 50%; (**a**) power estimated by model at various blade pitch angles and wind speed U; (**b**) power coefficient versus tip speed ratio at various blade pitch angles.

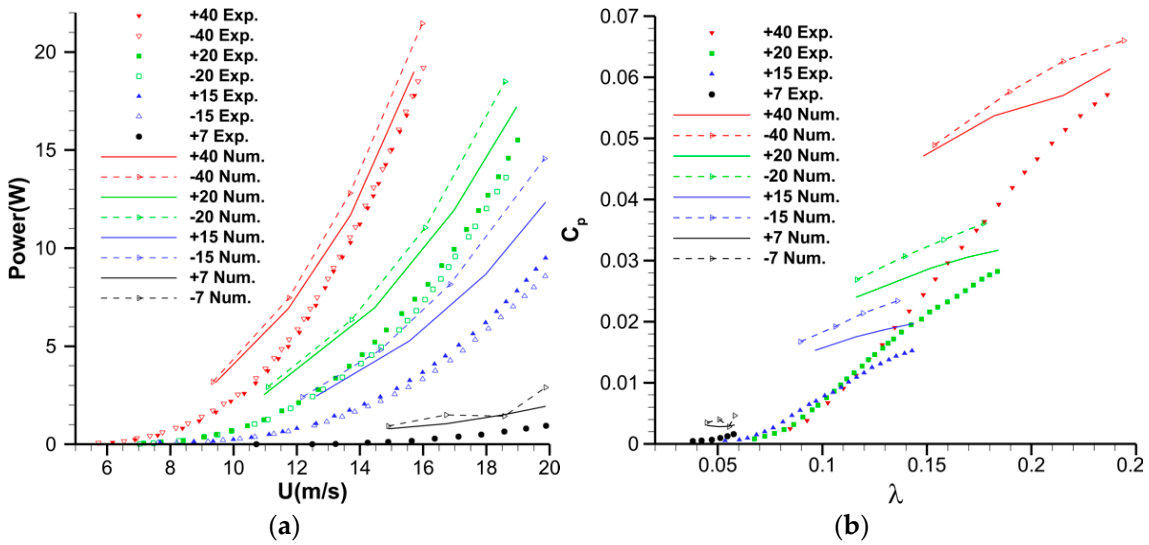

Figure 10. Estimation of turbine performance by CFDs model compared with experimental data when considering mechanical losses of 20%; (**a**) power estimated by model at various blade pitch angles and wind speed U; (**b**) power coefficient versus tip speed ratio at various blade pitch angles.

As mentioned before, two percentages related to the mechanical losses are considered; these arise from two factors: the meshing/simulation strategy and previous investigations comparing experimental and numerical results. Firstly, as was stated in Section 2.2, with the use of a symmetry boundary condition across the turbine's horizontal midplane (only considering half a turbine and no losses), the raw power output resulted in values of 50% smaller than full model. Secondly, from Howell et al. [26], it was identified that in order to compare the CFDs results of a whole turbine with experimental results, an error range of 20% must be considered, which was calculated after a series of tests on the experimental losses. Both cases highlight the requirement that a study be conducted on the mechanical losses of the turbine. Nonetheless, with the considered error range, the experimental results were possible to capture.

It is appreciable in Figure 9 that for most angle configurations with a low wind speed, the numerical estimation is close enough to the experimental results. In contrast, the 7° cases, which showed overestimations throughout the results, constituted an exception; this can be attributed to the low tip speed ratio regime, under which these two cases were operated, as can be seen in Figure 9b. At a high wind speed, a considerable underestimation was made for the 40° and 20° cases (corresponding to the highest λ values). Conversely, Figure 10b provides an estimation closer to the experimental results for the mentioned cases. We predict that this is due to a more energetic flow present at high λ values. This indicates that a turbulence model able to simulate a variation in energy may provide better results than the fully turbulent k-ω SST model. The losses accounted for can be seen indirectly as the modelling of a laminar or turbulent flow; i.e., as the percentage is lower, a more turbulent flow is considered. Clearly, this is a rough approximation but provides a good understanding of why implementing a laminar-to-turbulent model, such as the four-equation Transition SST model, can provide better results along the whole λ range. After the calibration of transition model coefficients, the investigations of Bianchini et al. [39] support this concept.

Further improvement can be achieved through the use of DDES or LES models, even for low λ values. This was confirmed by the works of Elkhoury et al. [31], where an investigation in low tip speed ratios (less than 0.3) was performed. However, such approaches are shown to result in high computational time requirements. In summary of the points mentioned, a better comprehension of the mechanical losses may result in a more reliable model. Nevertheless, in both Figures 9 and 10, the trend suggests that the

model is able to capture essential parts of the flow, especially for relatively high tip speed ratios (>0.15). In the following sections, the torque evolution computed by the model is discussed in further detail.

3.2. Torque

From Figure 11, irregular fluctuations are observed within the results of the +20° and +15° angles. As the velocity increases, a greater torque amplitude is witnessed. The inverse effect is realised across the +40° cases; amplitude is shown to decrease and fluctuations are shown to be sinusoidal.

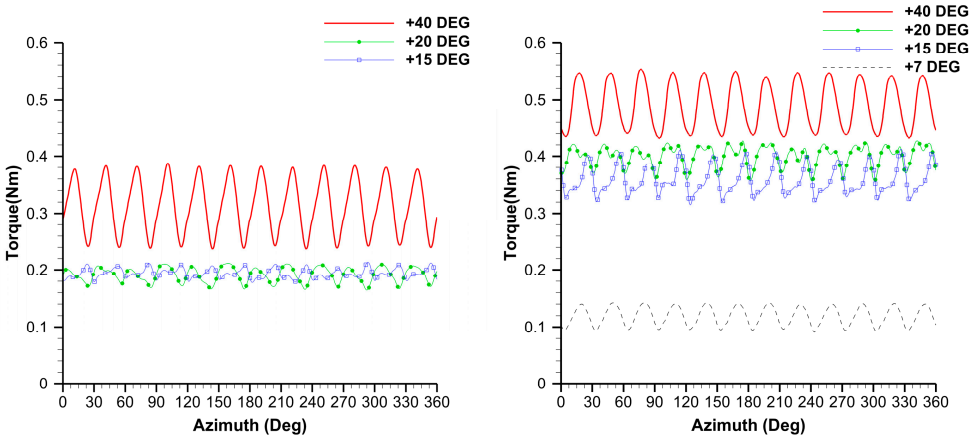

(**a**) (**b**)

Figure 11. Overall torque evolution for fourth revolution versus azimuth for positive blade pitch; (**a**) stream velocity of 11.7 m/s; (**b**) stream velocity of 16.8 m/s.

Similar results are obtained for negative pitch angles as shown in Figure 12; however, an inverse trend is observed for the negative 40 blade pitch angle. Results remain sinusoidal with an increase in amplitude.

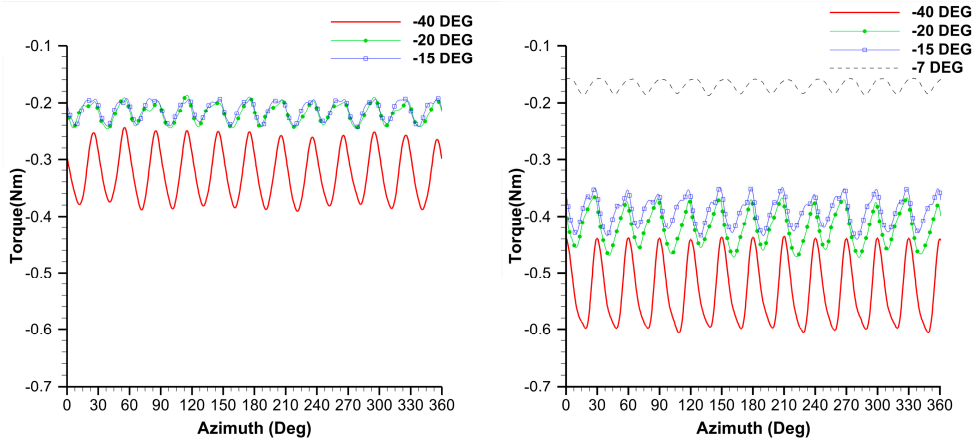

(**a**) (**b**)

Figure 12. Overall torque evolution for fourth revolution versus azimuth for negative blade pitch; (**a**) stream velocity of 11.7 m/s; (**b**) stream velocity of 16.8 m/s.

In a comparison of both positive and negative 7° pitch angles (at 16.8 m/s), sinusoidal torque signals are present in Figures 13 and 14. Note that positive and negative 7° pitch angles were not investigated for 11.7 m/s velocity due to the unavailability of data for comparison from the reference [19], as is explained in Table 5.

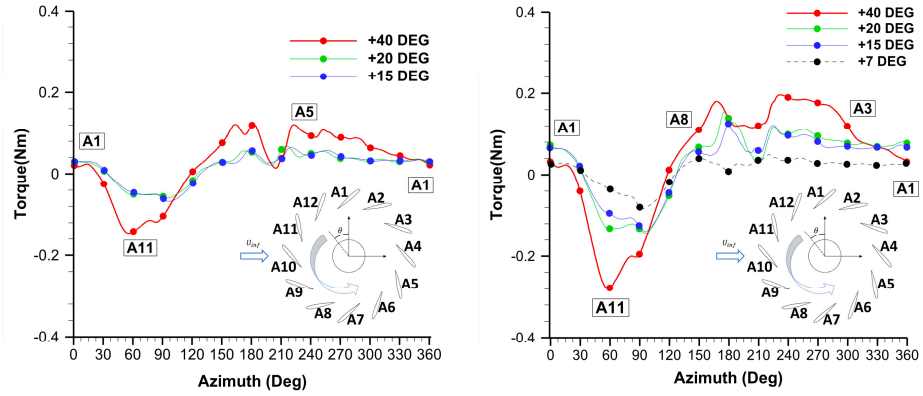

Figure 13. Torque on single airfoil for fourth revolution for positive blade pitch; (**a**) stream velocity of 11.7 m/s; (**b**) stream velocity of 16.8 m/s.

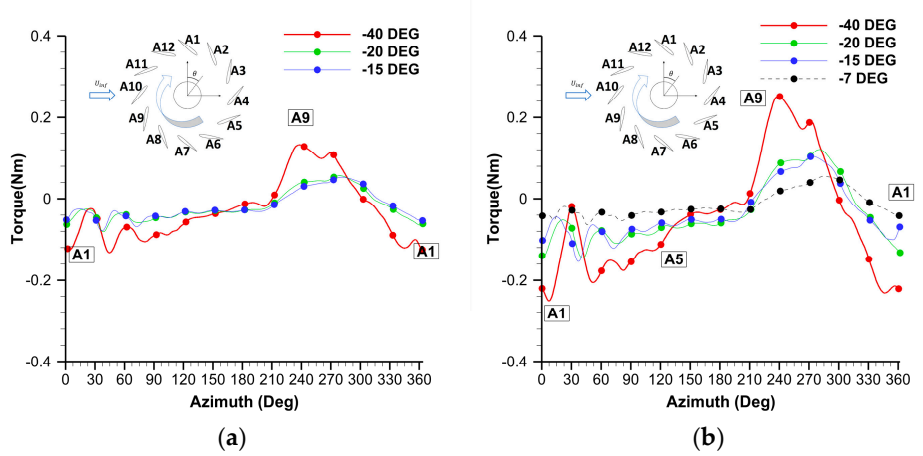

Figure 14. Torque on single airfoil for fourth revolution for negative blade pitch; (**a**) stream velocity of 11.7 m/s; (**b**) stream velocity of 16.8 m/s.

Torque signals were measured for a single airfoil in accordance with the azimuth angle. In Figure 13, the development of torque over the course of a complete revolution for positive blade pitch angles can be observed. At the initial stage, between 0 and 90°, torque is shown to increase with a decrease in blade angle, with a minimum peak torque value within the range of 60° to 90°. Above 90°, the maximum values of torque are reported; as blade pitches increase, a higher torque output is obtained. As the airfoil approaches the region of 80–210°, a sudden drop in torque is realised.

As expected, negative blade pitch angles are shown in Figure 14 to present a quasi-symmetric mirror of the positive results. The locations of maximum and minimum peak torque values are around 240° and 10–45°. In this instance, maximum values are observed to negatively impact turbine performance. The initial torque value for negative pitch angles is shown to be significantly lower than for positive angles. An example of the preceding statement can be described in the comparison of case 2, where torque values of 0 and −0.2 correspond to positive and negative blade pitch angles, respectively. In the next section, we appreciate the connection that can be made between the torque signal and velocity contours, and establish relevant flow phenomena in the close proximity and wake regions of the turbine.

3.3. Velocity

Figures 15–18 show the normalised air velocity profiles in the XZ and XY planes. Velocities are recorded at several different downstream locations in the assessment of the distance where the next turbine remains unaffected by the wake structure. Several numerical studies

have shown that the distance between two VAWTs in series has a direct relationship with the power coefficient and, accordingly, efficiency [40]. In addition, the performance of different configurations in offshore VAWT farm clustering was evaluated [41]. The results of this study conclude that vertical axis wind turbines can interact in a complementary manner when placed in close spacing (within the turbine wake).

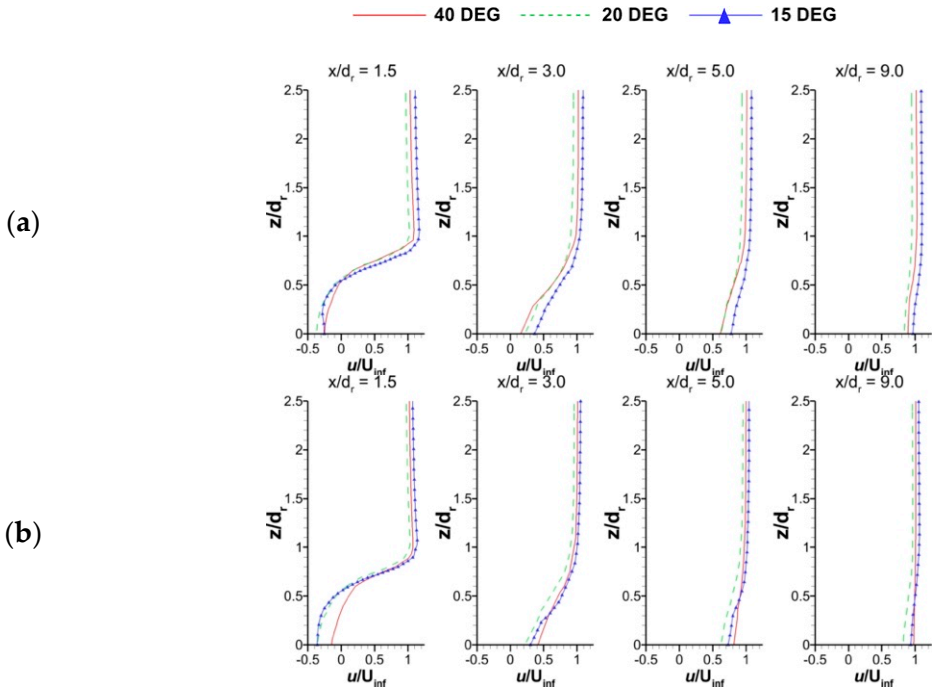

Figure 15. XZ mean velocity profiles for stream velocity of 11.7 m/s at different normalised distances for (**a**) positive pitch angles; (**b**) negative pitch angles.

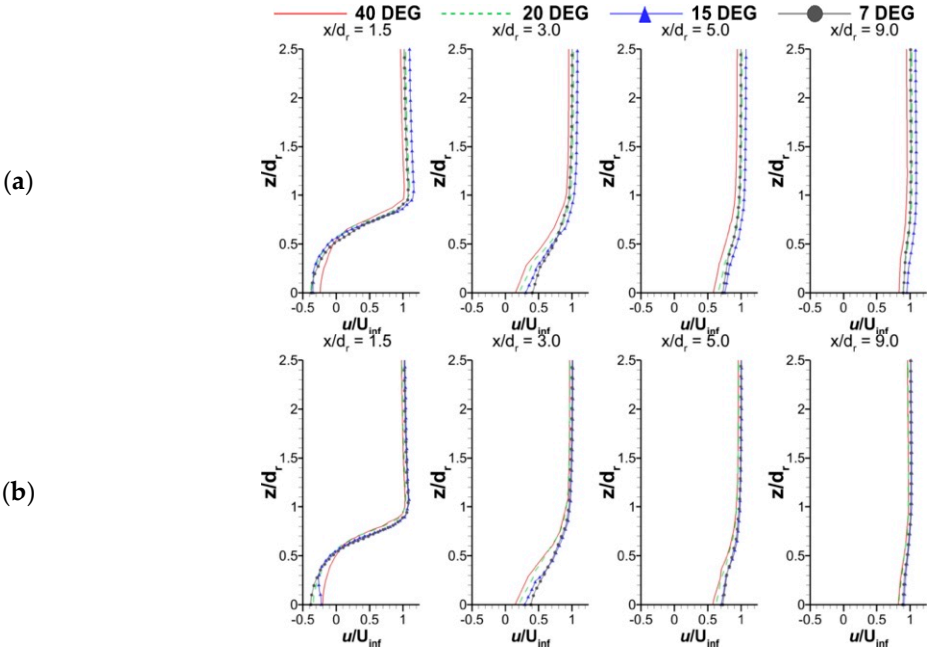

Figure 16. XZ mean velocity profiles for stream velocity of 16.8 m/s at different normalised distances for (**a**) positive pitch angles; (**b**) negative pitch angles.

(**a**)

(**b**)

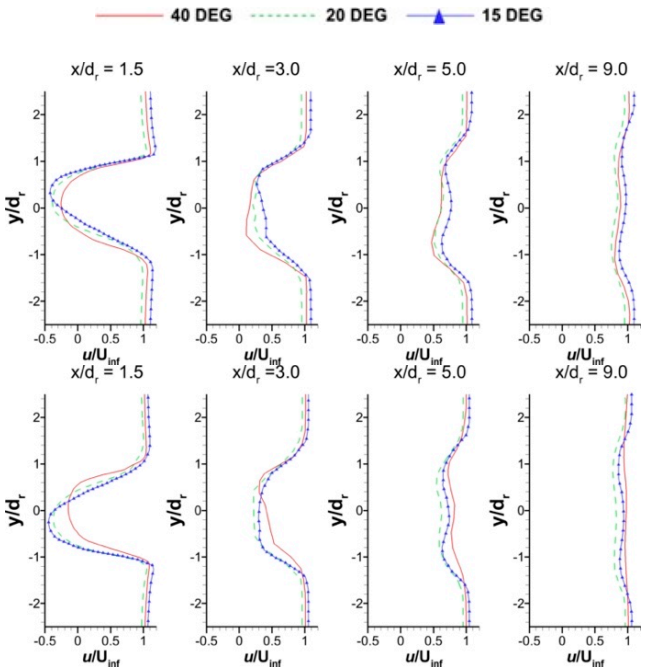

Figure 17. XY mean velocity profiles for stream velocity of 11.7 m/s at different normalised distances for (**a**) positive pitch angles; (**b**) negative pitch angles.

(**a**)

(**b**)

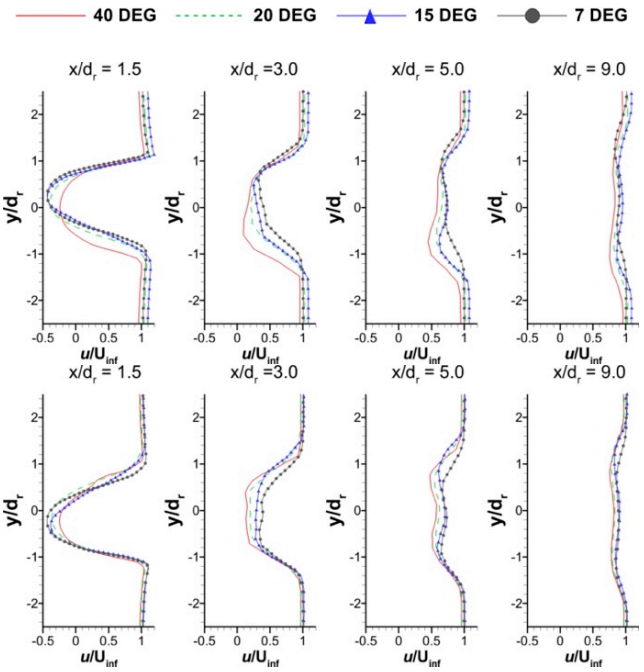

Figure 18. XY mean velocity profiles for stream velocity of 16.8 m/s at different normalised distances for (**a**) positive pitch angles; (**b**) negative pitch angles.

From the results, we identify a clear pattern for both the positive and negative pitch angles. At a distance of nine times the diameter of the turbine, a wake recovery is observed with a constant stream velocity profile, and beyond this distance, the airflow is recovered. This distance is met with agreement in the results of Vieira et al., where the wake recovery was recorded to be approximately ten times the turbine diameter [40]. Further agreement is seen within the numerically obtained results from Hezaveh et al., where wake recovery was found at distances between ten and twenty times the turbine diameter [41].

As can be observed in Figures 17 and 18, a shift in the velocity profile is observed close to the turbine (1.5 times the diameter) due to the rotation direction. For high values of the blade pitch angle, the flow rate inside the turbine increases, which consequently reduces the shift in velocity profile, which we predict is due to the alignment of flow. Comparing the blade angles studied in this work, a clear difference is recognised within the 40° cases, observing almost no shift in the low-velocity case. As the free stream velocity increases, the velocity profile of the 40° case becomes shifted, which we predict is related to the increased blockage effect that the rotating flow experiences.

In the XY plane, the wake exceeds the turbine diameter by roughly 200%, and for the pitch angle of 40 degrees, the recirculation is oriented to opposite sides due to the effect of the orientation of the blades (as shown in Figures 19 and 20). On the other hand, for other angles considered, the recirculation appears centred on the *x*-axis. This confirms that a considerable increase in the pitch angle influences the location of the vortical structure at the rear of the wind turbine.

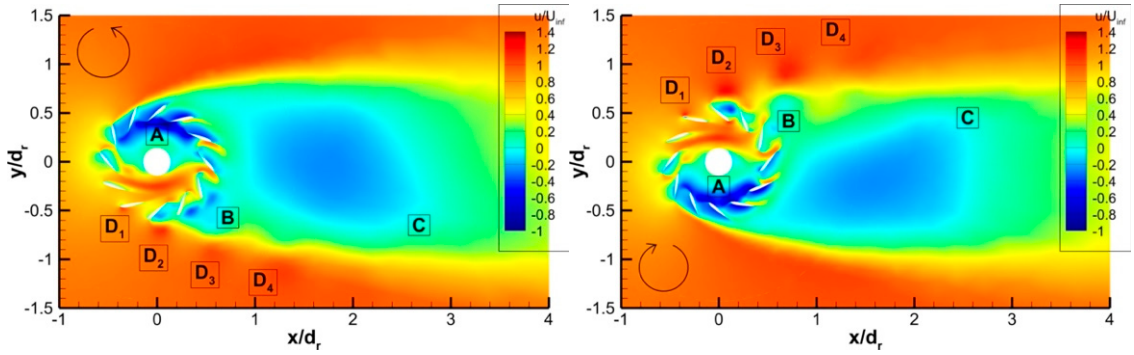

Figure 19. Instantaneous XY velocity contours for a stream velocity of 16.8 m/s for (**a**) +40, (**b**) −40 pitch angles.

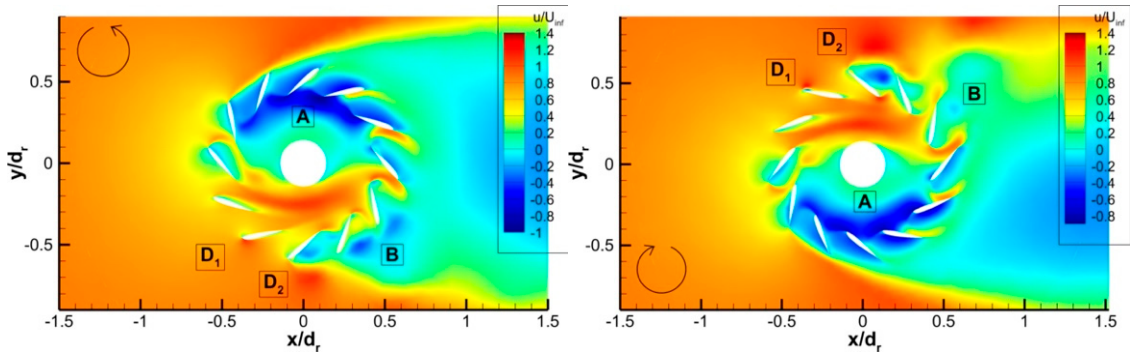

Figure 20. A close up of instantaneous XY velocity contours for a stream velocity of 16.8 m/s for (**a**) +40, (**b**) −40 pitch angles.

From the contour plots in Figures 19 and 20, it is possible to see that the blade orientation has a direct influence on the flow structures occurring inside the turbine and in its surrounding area. Firstly, the recirculation zone (A) can be confirmed within the turbine with negative velocities, and on the opposite side, the flow is accelerated, shown inversely between positive and negative pitch angles. As can be seen concerning the variation in torque with respect to the azimuth angle in Figures 13 and 14, the positions of the blades that generate the most torque are the airfoils located on the opposite side of the recirculation area, which confirms that with an increase in velocity, more torque is generated. Furthermore, in addition to the speed, the position of the blade with respect to the wind

direction has a direct relationship with torque generation, which is why the blades located in the area opposite to the recirculation zone generate different amounts of torque, even if they are exposed to a wind flow with a similar speed.

At the leeward side of the turbine, eddies are created, which, as seen inside the turbine, are placed on opposite sides (B), depending on the pitch orientation. Regarding the wake, it is possible to confirm that the recirculation region at the rear of the VAWT is oriented towards one side (C) due to the pitch angle orientation. In addition, in both cases, there are some vortical structures shed through the rotary motion of the turbine, where an acceleration of the flow can be seen (D). Four vortical structures are generated in both cases, where the velocity is higher than the stream velocity.

When analysing the XZ plane depicted in Figure 21, similar velocities are observed for both positive and negative pitch angles. Recirculation is observed to occur at the top of the endplate (E) due to the collision of the flow against the obstacle; this happens in a similar way for both positive and negative pitch angles. Subsequently, the collision flow separates and further proceeds to quickly reattach, giving rise to the formation of a horseshoe vortex. In addition, due to the flow separation at the front of the turbine (in the positive direction of the x-axis), an acceleration of the flow is observed, reaching (normalised) velocities higher than those of the wind stream velocity (1.17 for $+40^{\circ}$ and 1.19 for -40°).

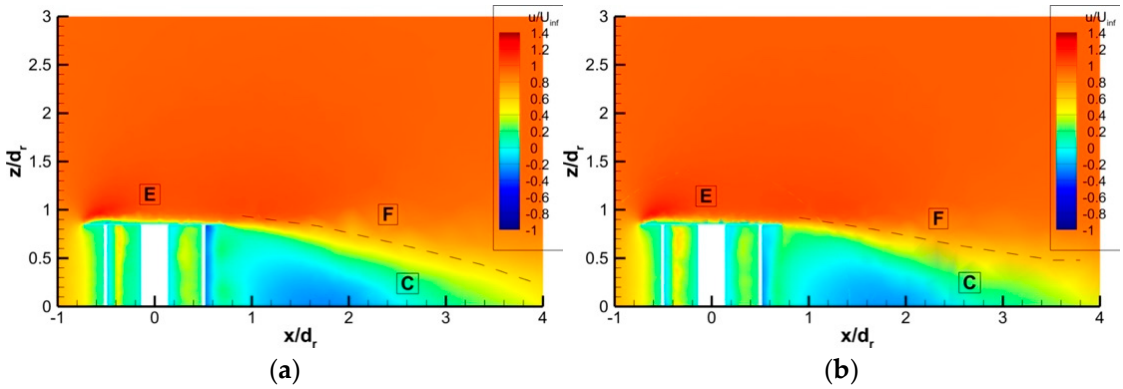

Figure 21. Instantaneous XZ velocity contours for a stream velocity of 16.8 m/s for (**a**) +40; (**b**) −40 pitch angles.

The effect of the endplate on the wake is further confirmed to limit the turbulent zone at the turbine height. In this area, it is visible that for positive pitch angle blades, a clearer shear layer (F) is obtained compared to negative pitch angles, which is due to a tidier flow for the turbine with positive pitch angles compared to negative. This effect can be seen in better detail in the figures with the streamlines. Subsequently, the streamlines for both cases with positive and negative pitch angles are shown in Figures 22–26, presenting a visualisation of the flow structures that are created close to the wind turbine.

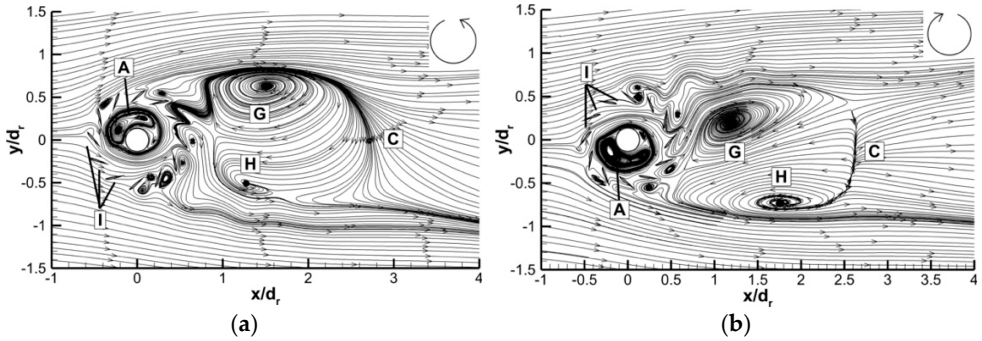

Figure 22. Symmetry plane streamlines for a stream velocity of 16.8 m/s for (**a**) +40; (**b**) −40 pitch angles.

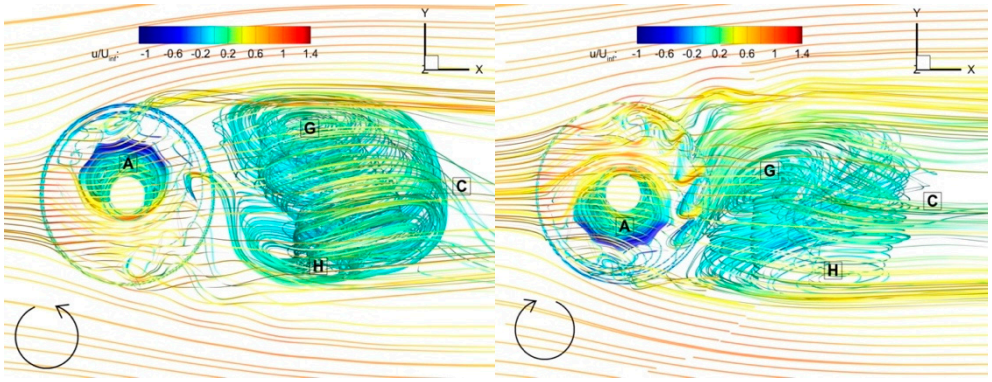

(**a**) (**b**)

Figure 23. Symme3D Streamlines (XY top view) for a stream velocity of 16.8 m/s for (**a**) +40; (**b**) −40 pitch angles.

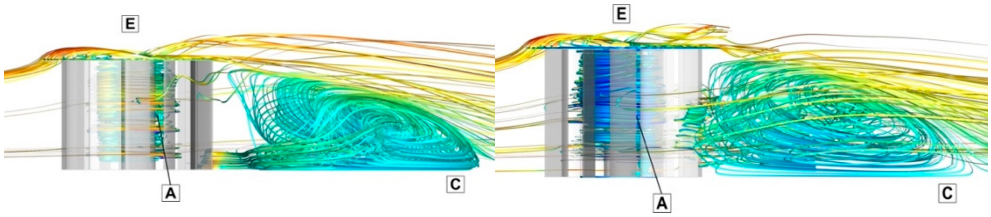

(**a**) (**b**)

Figure 24. D Streamlines (XZ side view) for a stream velocity of 16.8 m/s for (**a**) +40; (**b**) −40 pitch angles.

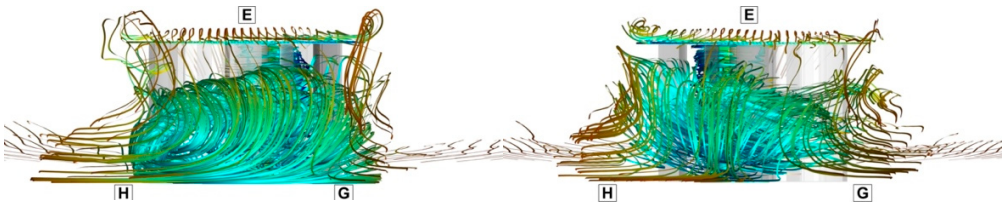

(**a**) (**b**)

Figure 25. D Streamlines (YZ side view) for a stream velocity of 16.8 m/s for (**a**) +40; (**b**) −40 pitch angles.

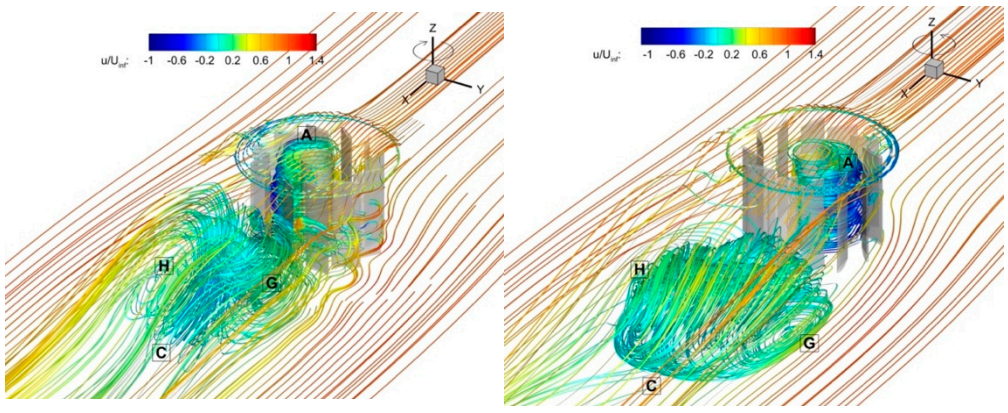

(**a**) (**b**)

Figure 26. D Streamlines for a stream velocity of 16.8 m/s for (**a**) +40; (**b**) −40 pitch angles.

Figure 22 shows the streamlines in the symmetry plane, where two major differences between the positive and negative pitch angles are noticed. Firstly, as previously mentioned, the flow structures inside the turbine are confirmed. Recirculation (A) due to the effect of the inner cylinder wall is shown to occur on the opposite side due to the direction of

rotation. Again, we confirm that the recirculation zone behind the turbine for both cases reaches up to approximately 2.6 times the turbine diameter (C). In addition, the creation of small vortices in the close areas of the airfoils is appreciable, except for aerofoils 8-9-10 (I) for positive pitch angles and 10-11-12 (I) for negative pitch angles, where no vortices were created due to the direct incidence of the air flow and the position of the blades. A quasi-symmetric behaviour is observed between both configurations.

As for the recirculation zone, the symmetry plane depicts two large vortical structure centres (G and H) for both directions of rotation. The centre located at 'G' is shown at the left rear of the turbine and 'H' is taken at the right back side of the turbine for both directions of rotation. With further 3D analysis (Figures 23–26), it can be noted that these two vortical structure centres (G and H) interact with each other with great complexity, producing a large 3D vortical structure. The shape of this structure is determined differently depending on the rotation of the turbine, where for clockwise rotation, the flow seems to be more organised.

From Figures 23–26, a clear difference is confirmed between the vortical structures within both turbine and wake regions. In summary of the points discussed within this section, the following was observed. As flow collides with the endplate, separation is realised and is immediately followed by a sharp reattachment of the flow and was further shown to lead to the creation of a horseshoe vortex (J). A three-dimensional vortical structure occurring inside the turbine (A), which starts at the symmetry plane and ends at the endplate, could be clearly observed. Comparing positive and negative pitch angles, in both cases, the vortical structure behind the turbine was shown to be restricted by the endplate and to descend to the point 'C', where the recirculation region ended.

3.4. Pressure

The pressure distribution close to the turbine in the symmetry plane is shown in Figure 27. In both cases, the low-pressure zones (A) are observed close to several airfoils and relate to regions of maximum torque generation (Figures 13b and 14b). Considering the positive pitch angle case, the azimuth position associated with airfoil 5 is shown to generate the highest torque output. This can be seen with the difference in pressure between the inner and outer surfaces; the same occurs for airfoil 6 and 7 to a smaller extent, as is apparent in the size reduction in the low-pressure zone. As shown in Figure 27b, a similar behaviour is observed for the negative blade angle.

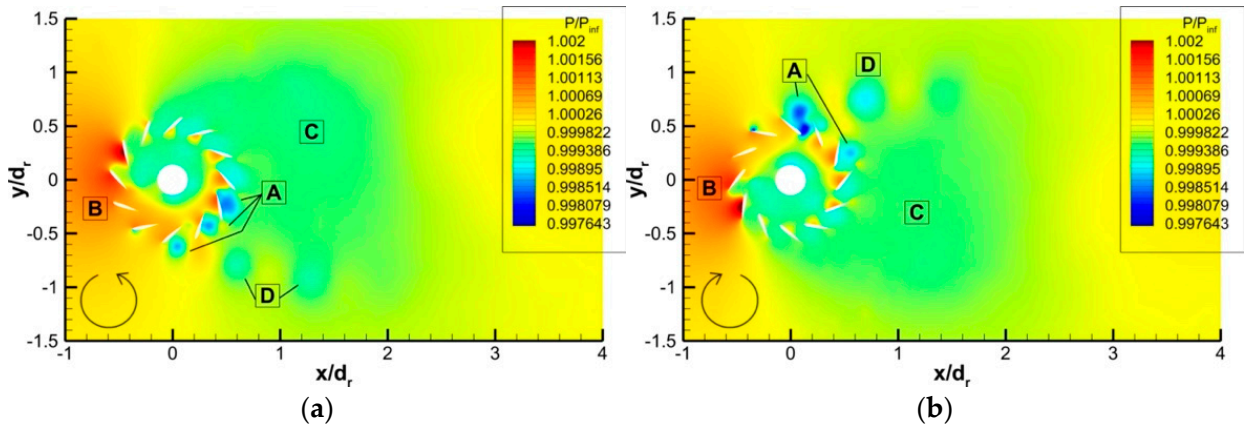

Figure 27. XY pressure contour for stream velocity of 16.8 m/s for (**a**) +40; (**b**) −40 pitch angles.

The cylinder is surrounded by a low-pressure zone, and is associated with the recirculation zone found within the streamline visualisations of Figure 22. As previously mentioned, the freestream flow contributes to the formation of the recirculation region. In this way, a high-velocity region in close proximity to the inner cylinder can be associated with the low-pressure region, as demonstrated in the comparison of Figure 27a,b. At the windward side of the turbine, a high-pressure zone developed (B) as a consequence of the

blockage effect of the airfoil blades on the airflow. This resulted in the generation of an adverse torque, mainly by the three aerofoils which were encountered as soon as the air approached the turbine, whereby, in this instance, airfoils 9 and 11 are found to be the main contributors to this effect (dependent on the direction of rotation).

As the turbine rotates, regions of high velocity are shed from the retreating side ($180^\circ < \theta < 270^\circ$) towards the freestream, as shown in Figure 19. The same pattern is visible in the pressure distribution through the low-pressure regions, identified as 'D' in Figure 27. These zones are attributed to the air within close proximity of each aerofoil's suction side, which are advected downstream with an increase in pressure until freestream values are reached. From Figures 27 and 28, the recirculation zone (C) is identified as a large area of low pressure for both blade orientations. By looking at the XZ pressure distribution (Figure 28), some structures mentioned above are observed from a different plane. In agreement with the velocity contours, the air impinges the turbine endplate, resulting in a small recirculation zone (E).

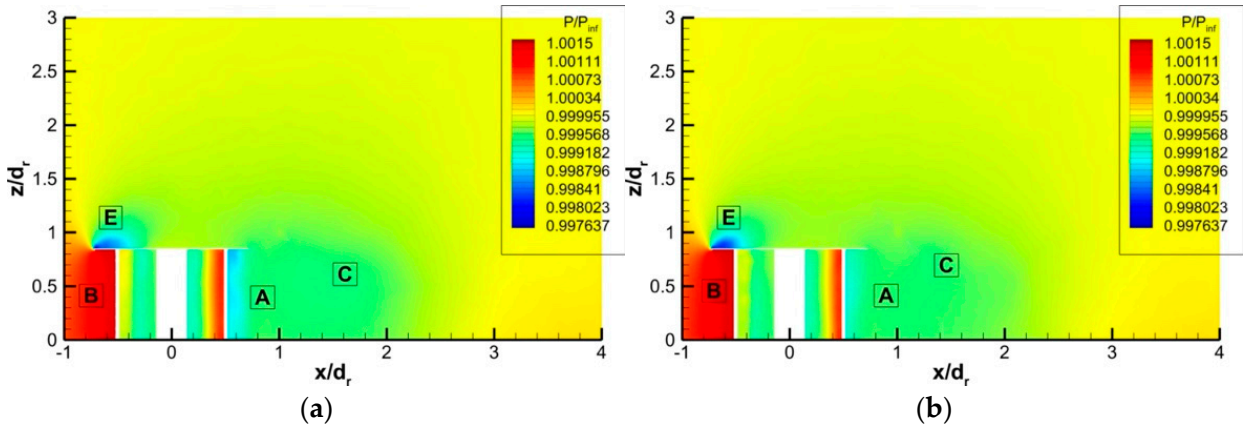

Figure 28. XZ pressure contour for stream velocity of 16.8 m/s for (**a**) +40; (**b**) −40 pitch angles.

3.5. Turbulent Kinetik Energy (TKE)

The turbulent kinetic energy (TKE) results measure the magnitude of Reynolds stresses, thus determining a quantifiable value of turbulence within the Farrah wind turbine. Figures 29–32 agree with streamline results, where turbulent hotspots are apparent within the upstream region above the endplate, downstream from the aerofoil vortex shedding, and at a slight distance from the turbine within the wake.

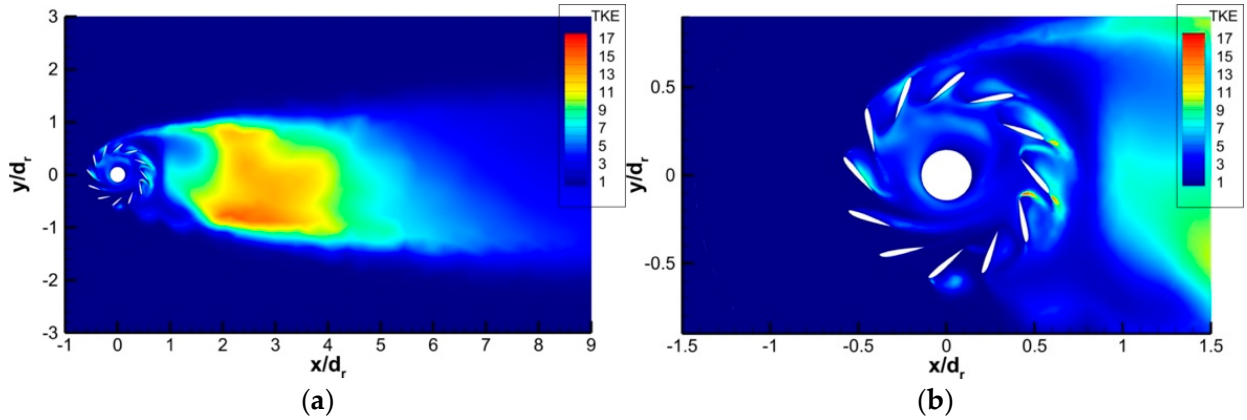

Figure 29. Instantaneous TKE representation in XY plane for +40° case: (**a**) wake view; (**b**) zoom view of turbine.

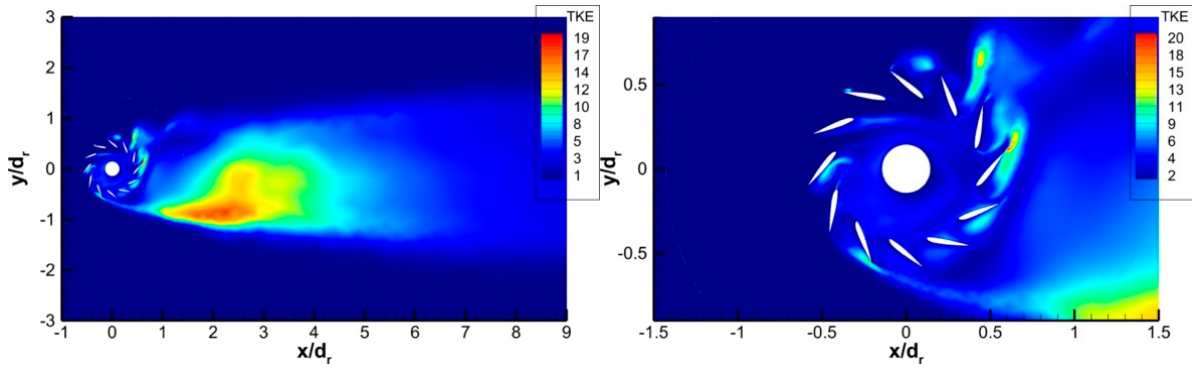

(**a**) (**b**)

Figure 30. Instantaneous TKE representation in XY plane for −40° case: (**a**) wake view; (**b**) zoom view of turbine.

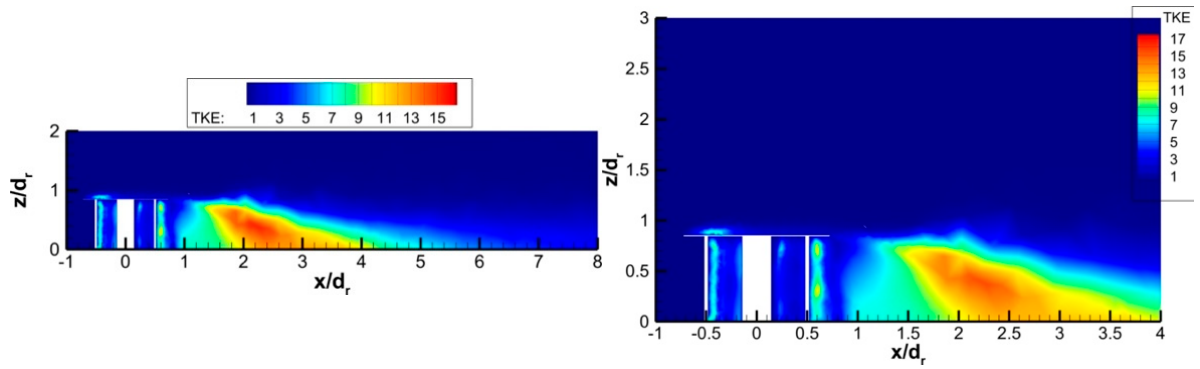

(**a**) (**b**)

Figure 31. Instantaneous TKE representation in XZ plane for +40° case: (**a**) wake view; (**b**) zoom view of turbine.

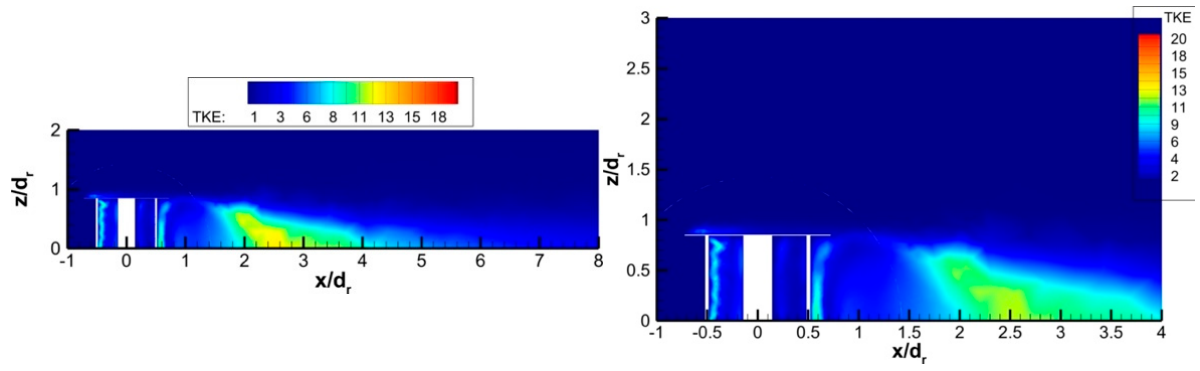

(**a**) (**b**)

Figure 32. Instantaneous TKE representation in XZ plane for −40° case: (**a**) wake view; (**b**) zoom view of turbine.

From the instantaneous results shown, significantly smaller values of TKE within the turbine are reported in comparison with the two identified hotspot locations. We expect that TKE is advected through the present vortex shedding of the full turbine and individual aerofoils, which can be attributed to the wake structure of greater magnitude (approximately 2 m from the centre). Following the TKE results discussed, a 3D Q-criterion analysis is carried out, providing further understanding into the relevant vortical structures.

3.6. Q-Criterion

Figures 33 and 34 show the Q-criterion results, identifying key locations of vorticity in the fluid flow, and the colour map, ranging from negative to positive values, indicates regions of different flow velocities. The vortices visualised here likely originate from the interaction of the flow with the aerofoils of the turbine. As the blades move through the flow, especially at the trailing edges, boundary layer separation occurs. This separation induces the formation of vortices due to shear and adverse pressure gradients, as shown in #1 in Figure 33a.

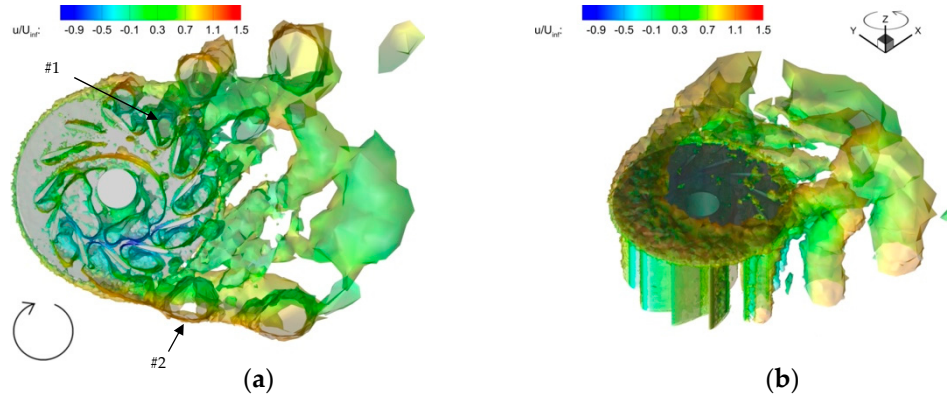

Figure 33. Q-criterion representation for +40° and stream velocity of 16.8 m/s: (**a**) bottom view; (**b**) isometric view.

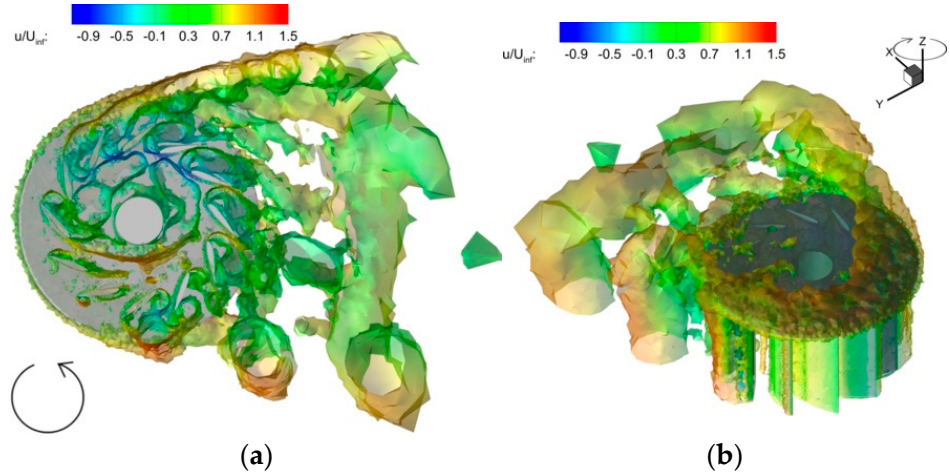

Figure 34. Q-criterion representation for −40° and stream velocity of 16.8 m/s: (**a**) bottom view; (**b**) isometric view.

These figures also highlight the role of the endplate, which is commonly used to control the flow around the blades, reduce tip vortices, and increase the overall aerodynamic efficiency. #2 in Figure 33a shows concentrated areas of vorticity, suggesting that the endplate influences the vortex dynamics around the blade tips and trailing edges.

Once again, the horseshoe vortex can be seen, on which we expected to see von Kármán street effects over time.

4. Conclusions

In this study, the turbulent flow dynamics (Re = 5×10^3 to Re = 1×10^5) around a vertical axis wind turbine (VAWT) of the Farrah type were investigated, based on the experimental work of Prince et al. [19]. The first goal was to validate the numerical model using the Spalart–Allmaras (S-A) and k-ω SST turbulence models. A mesh convergence

analysis showed that a 14-million-element mesh provided optimal results while the k-ω SST model proved more accurate, with errors of 4.02%, compared to 43.25% for the S-A model for this particular investigation.

Simulations were conducted for pitch angles of 7°, 15°, 20° and 40°, in both positive and negative orientations, with which we analysed power generation, torque evolution and flow dynamics. The model captured the exponential trends from the experimental data, where power increased with both pitch angle and wind speed. Negative pitch angles resulted in a slightly higher power output.

Comparing single and multiple boundary condition configurations revealed that the latter improved accuracy in flow visualisation and power output. Torque analysis showed that all aerofoils generated equal torque during a full revolution, with a 30° offset corresponding to the spacing between aerofoils. A high torque was linked to specific velocity and pressure contour hotspots.

Flow analysis identified recirculation regions and differences between positive and negative rotations. The model captured endplate separation and the associated horseshoe vortex. For both positive and negative cases at 40°, quasi-symmetric differences in the inner turbine and wake recirculation zones were observed, with the wake extending up to 2.6 times the turbine diameter.

Velocity profiles in the wake were similar across all pitch angles and directions, with wake recovery at nine times the turbine diameter. A shift in wake velocity near the turbine was noted due to its rotation, decreasing as the gap between aerofoils increased. At higher freestream velocities, a blockage effect reduced flow through the turbine, causing a more significant wake velocity shift.

Torque output was influenced by pressure distribution near the aerofoils. High-pressure regions due to blockage reduced torque, while low-pressure zones on the retreating side enhanced it. The suction-side low-pressure spots, which were shed during turbine rotation, contributed to torque production until pressure equilibrium was achieved.

Turbulence was quantified using TKE contour visualisations, with high turbulence levels found at the upstream endplate, downstream aerofoils and wake recirculation zones. Lower turbulence was observed near the inner cylinder, with 3D iso-surfaces of the q-criterion highlighting vorticity.

The numerical model was validated against experimental results, providing insights into the effects of pitch angles and aerofoil orientation on torque, power and flow dynamics. However, use of the k-ω Transitional SST model is suggested for future work, as the current fully turbulent model may overestimate power due to the transitional Reynolds range. Future research should focus on optimising aerofoil design by studying lift and drag variations and analysing the effect of aerofoil number on power generation for better performance and material savings.

Author Contributions: Conceptualization, C.S.B. and Z.A.R.; methodology, C.S.B.; software, C.S.B.; validation, C.S.B., Z.A.R. and S.A.P.; formal analysis, C.S.B.; investigation, C.S.B.; data curation, Z.A.R.; writing—original draft preparation, C.S.B.; writing—review and editing, C.S.B. and Z.A.R.; visualisation, C.S.B.; supervision, Z.A.R. and S.A.P.; project administration, Z.A.R. All authors have read and agreed to the published version of the manuscript.

Funding: This research received no external funding.

Data Availability Statement: Data are contained within the article.

Acknowledgments: The numerical solution was performed with the help of the Cranfield High-Performance (HPC) facility. We acknowledge the technical support from the Cranfield HPC team during the research.

Conflicts of Interest: The authors declare no conflicts of interest.

Abbreviations

CFD	Computational Fluid Dynamics
DDES	Delay Detached Eddy Simulation
HAWT	Horizontal Axis Wind Turbine
LES	Large Eddy Simulation
RANS	Reynolds-Averaged Navier–Stokes
TKE	Turbulent Kinetic Energy
VAWT	Vertical Axis Wind Turbine
URANS	Unsteady Reynoleds-Averaged Navier–Stokes

References

1. UK Government. *The Carbon Plan: Delivering Our Low Carbon Future*; UK Government: London, UK, 2011.
2. International Energy Agency. *Net Zero by 2050*; IEA: Paris, France, 2021.
3. Office of National Statistics. *Wind Energy in the UK*; ONS: Newport, Wales, 2021.
4. Patel, S. Changing Winds: The Evolving Wind Turbine. *Power* **2011**, *155*, 38–44.
5. Spera, D.A. *Wind Turbine Technology: Fundamental Concepts in Wind Turbine Engineering*; ASME Press: New York, NY, USA, 2009; ISBN 9780791802601.
6. Mertens, S. *Wind Energy in the Built Environment*; Multi Science Publishing Company: Brentwood, UK, 2005.
7. Ferreira, C.S.; van Bussel, G.J.W.; van Kuik, G.A.M. 2D CFD simulation of dynamic stall on a vertical axis wind turbine: Verification and validation with PIV measurements. In Proceedings of the 45th AIAA Aerospace Sciences Meeting, Reno, NV, USA, 8–11 January 2007; pp. 16191–16201.
8. Hofemann, C.; Ferreira, C.S.; Dixon, K.; van Bussel, G.J.W.; van Kuik, G.A.M.; Scarano, F. 3D Stereo PIV Study of Tip Vortex Evolution on a Vawt. 2008, pp. 1–8. Available online: https://repository.tudelft.nl/record/uuid:7a500ed8-586c-40da-af62-3cd65d5e3bfe (accessed on 29 October 2024).
9. Wood, D. *Small Wind Turbines, Analysis, Design, and Application*; Springer: London, UK, 2011.
10. Savonius, S. *The Wing Rotor in Theory and Practice*; Savonius: Helsinki, Finland, 1928.
11. Savonius, S. The S-rotor and its applications. *Mech. Eng.* **1931**, *53*, 333–338.
12. Bach, G. Untersuchungen über Savonius-Rotoren und verwandte Strömungsmaschinen. *Forsch. Auf Dem Geb. Des Ingenieurwesens A* **1931**, *2*, 218–231. [CrossRef]
13. Fujusawa, N.; Gotoh, F. Pressure measurements and flow visualisation study of a Savonius rotor. *J. Wind Eng. Ind. Aerodyn.* **1992**, *39*, 51–60. [CrossRef]
14. Fujusawa, N. Velocity measurements and numerical calculations of flow fields in and around Savonius rotors. *J. Wind Eng. Ind. Aerodyn.* **1996**, *59*, 39–50. [CrossRef]
15. Dobrev, I.; Massouha, F. CFD and PIV investigation of unsteady flow through Savonius wind turbine. *Energy Procedia* **2001**, *6*, 711–720. [CrossRef]
16. McWilliam, M.; Johnson, D. Velocity measurements of flow around model vertical axis wind turbines. *Int. J. Green Energy* **2008**, *5*, 55–68. [CrossRef]
17. Can, K.; Feng, Z.; Xuejun, M. Comparison Study of a Vertical-Axis Spiral Rotor and a Conventional Savonius Rotor. In Proceedings of the 2010 Asia-Pacific Power and Energy Engineering Conference (APPEEC), Chengdu, China, 28–31 March 2010; pp. 1–4.
18. Kumbernuss, J.; Chen, J.; Yang, H. Investigation into the relationship of the overlap ratio and shift angle of double stage three bladed vertical axis wind turbine (VAWT). *J. Wind Eng. Ind. Aerodyn.* **2012**, *107–108*, 57–75. [CrossRef]
19. Prince, S.A.; Badalamenti, C.; Georgiev, D. Experimental investigation of a variable geometry vertical axis wind turbine. *Wind Eng.* **2021**, *45*, 904–920. [CrossRef]
20. Arrondeau, B.; Rana, Z.A. Computational Aerodynamics Analysis of Non-Symmetric Multi-Element Wing in Ground Effect with Humpback Whale Flipper Tubercles. *Fluids* **2020**, *5*, 247. [CrossRef]
21. Castro, X.; Rana, Z. Aerodynamic and Structural Design of a 2022 Formula One Front Wing Assembly. *Fluids* **2020**, *5*, 237. [CrossRef]
22. Bagul, P.; Rana, Z.A.; Jenkins, K.W.; Könözsy, L. Computational engineering analysis of external geometrical modifications on MQ-1 unmanned combat aerial vehicle. *Chin. J. Aeronaut.* **2020**, *33*, 1154–1165. [CrossRef]
23. Bang, C.S.; Rana, Z.A.; Konozsy, L.; Rodriguez, V.M.; Temple, C. Aeroelastic Analysis of a Single Element Composite Wing in Ground Effect Using Fluid Structure Interaction. *J. Fluids Eng.* **2021**, *144*, 041202. [CrossRef]
24. Bang, C.S.; Rana, Z.A.; Konozy, L.; Rodriguez, V.M.; Temple, C. Numerical Investigation and Fluid-Structure Interaction (FSI) Analysis on a Double-Element Simplified Formula One (F1) Composite Wing in the Presence of Ground Effect. *Fluids* **2022**, *7*, 85. [CrossRef]
25. Ghasemian, M.; Ashrafi, Z.N.; Sedaghat, A. A review on computational fluid dynamic simulation techniques for darrieus vertical axis wind turbines. *Energy Convers. Manag.* **2017**, *149*, 87–100. [CrossRef]
26. Howell, R.; Qin, N.; Edwards, J.B.; Durrani, N.A. Wind tunnel and numerical study of a small vertical axis wind turbine. *Renew. Energy* **2010**, *35*, 412–422. [CrossRef]

27. Rossetti, A.; Pavesi, G. Comparison of different numerical approaches to the study of the h-darrieus turbines start-up. *Renew. Energy* **2013**, *50*, 7–19. [CrossRef]
28. Rezaeiha, A.; Kalkman, I.; Blocken, B. Cfd simulation of a vertical axis wind turbine operating at a moderate tip speed ratio: Guidelines for minimum domain size and azimuthal increment. *Renew. Energy* **2017**, *107*, 373–385. [CrossRef]
29. Rezaeiha, A.; Montazeri, H.; Blocken, B. Towards accurate cfd simulations of vertical axis wind turbines at different tip speed ratios and solidities: Guidelines for azimuthal increment, domain size and convergence. *Energy Convers. Manag.* **2017**, *156*, 301–316. [CrossRef]
30. Elkhoury, M.; Kiwata, T.; Aoun, E. Experimental and numerical investigation of a three-dimensional vertical-axis wind turbine with variable-pitch. *J. Wind Eng. Ind. Aerodyn.* **2015**, *139*, 111–123. [CrossRef]
31. Elkhoury, M.; Kiwata, T.; Nagao, K.; Kono, T.; Elhajj, F. Wind tunnel experiments and Delayed Detached Eddy Simulation of a three-bladed micro vertical axis wind turbine. *Renew. Energy* **2018**, *129*, 63–74. [CrossRef]
32. Liu, J.; Zhu, W.; Xiao, Z.; Sun, H.; Huang, Y.; Liu, Z. DDES with adaptive coefficient for stalled flows past a wind turbine airfoil. *Energy* **2018**, *161*, 846–858. [CrossRef]
33. Aerotoolbox. NACA 5 Series Airfoil Generator. Available online: https://aerotoolbox.com/naca-5-series-airfoil-generator/ (accessed on 28 September 2022).
34. ANSYS. *Ansys Fluent User's Guide*; ANSYS: Canonsburg, PA, USA, 2013.
35. Bruneau, C.H.; Tancogne, S. Far field boundary conditions for incompressible flows computation. *J. Appl. Anal. Comput.* **2018**, *8*, 690–709. [CrossRef]
36. Bedon, G.; Betta, S.D.; Benini, E. A computational assessment of the aerodynamic performance of a tilted darrieus wind turbine. *J. Wind Eng. Ind. Aerodyn.* **2015**, *145*, 263–269. [CrossRef]
37. Hassen, S.M.R.; Ali, M.; Islam, M.Q. The effect of solidity on the performance of h-rotor darrieus turbine. *AIP Conf. Proc.* **2016**, *1754*, 040012.
38. Lanzafame, R.; Mauro, S.; Messina, M. 2D CFD modeling of h-darrieus wind turbines using a transition turbulence model. In Proceedings of the Conference of the Italian Thermal Machines Engineering Association, Lecce, Italy, 6–8 September 2013.
39. Bianchini, A.; Balduzzi, F.; Bachant, P.; Ferrara, G.; Ferrari, L. Effectiveness of two-dimensional cfd simulations for darrieus vawts: A combined numerical and experimental assessment. *Energy Convers. Manag.* **2017**, *136*, 318–328. [CrossRef]
40. Vieira, R.S.; Rocha, L.A.O.; Isoldi, L.A.; Dos Santos, E.D. Numerical study of two vertical axis wind turbines Darrieus type line up in function of power coefficient. *Rev. Bras. Energias Renov.* **2017**, *6*, 346–359. [CrossRef]
41. Hezaveh, S.H.; Bou-Zeid, E.; Dabiri, J.; Kinzel, M.; Cortina, G.; Martinelli, L. Increasing the Power Production of Vertical-Axis Wind-Turbine Farms Using Synergistic Clustering. *Bound. Layer Meteorol.* **2018**, *169*, 275–296. [CrossRef]